

Evolution of structure and magnetic properties in electron-doped double perovskites, $\text{Sr}_{2-x}\text{La}_x\text{MnWO}_6$ ($0 \leq x \leq 1$)

Qisheng Lin^a, Martha Greenblatt^{a,*}, Mark Croft^b

^aDepartment of Chemistry and Chemical Biology, Rutgers, The State University of New Jersey, Piscataway, NJ 08854, USA

^bDepartment of Physics, Rutgers, The State University of New Jersey, Piscataway, NJ 08854, USA

Received 7 September 2004; received in revised form 7 December 2004; accepted 16 December 2004

Available online 13 March 2005

Abstract

Powder neutron and X-ray diffraction studies show that the double perovskites in the region $0 \leq x \leq 1$ exhibit two crystallographic modifications at room temperature: monoclinic $P2_1/n$ and tetragonal $I4/m$, with a boundary at $0.75 < x < 0.9$. Magnetic susceptibility measurements indicate that for $x = 0$ and 0.5 $\text{Sr}_{2-x}\text{La}_x\text{MnWO}_6$ orders antiferromagnetically (AFM) at 15 and 25 K, respectively, for $0.75 \leq x < 1.0$, a contribution of weak ferromagnetism (FM), probably due to canted-AFM order, increases with increasing x . The end point compound SrLaMnWO_6 shows the strongest FM cluster effect; however, no clear evidence of magnetic order is discernable down to 4.2 K. X-ray absorption spectroscopy (XAS) confirms Mn^{2+} and mixed-valent $\text{W}^{6+/5+}$ formal oxidation states in $\text{Sr}_{2-x}\text{La}_x\text{MnWO}_6$.

© 2005 Elsevier Inc. All rights reserved.

Keywords: $\text{Sr}_{2-x}\text{La}_x\text{MnWO}_6$; Double perovskite; Structure; Neutron diffraction; Magnetic properties

1. Introduction

The discovery of colossal-magnetoresistance properties at temperatures significantly above room temperature in the $\text{Sr}_2\text{FeMoO}_6$ double perovskite [1] stimulated the search for similar effects in related $A_2B'B''\text{O}_6$ -type double perovskites (where A is an alkaline-earth or rare-earth ion, and B' and B'' are different transition metal cations) [2–4], driven by the possible technological applications of these materials in magnetoelectronic devices. In general, the interesting physical properties of new perovskites are primarily due to the electronic interactions of B -site cations. For example, when Mo^{5+} (d^1) is substituted by Re^{6+} (d^1) in $\text{Sr}_2\text{FeMoO}_6$, a spin-dependent tunneling-type giant magnetoresistance, which persists up to room temperature in annealed samples, is observed [2].

Recently, in our search for new d^1-d^5 magnetic double perovskites, isoelectronic with $\text{Sr}_2\text{FeMoO}_6$, we have reported on $A\text{LaMnMoO}_6$ ($A = \text{Sr}, \text{Ba}$) [5,6]. BaLaMnMoO_6 crystallizes in a pseudo-cubic lattice ($I\bar{1}$, subgroup of $Fm\bar{3}m$) [5] with large intra-grain magnetoresistance behavior [6]. The onset of the magnetoresistance was found to be coincident with the spin-glass transition at ~ 25 K, and not associated with the ferrimagnetic transition observed at 145 K [5]. In contrast, the SrLaMnMoO_6 analog was found to crystallize in monoclinic ($P2_1/n$) space group with a significant tilting distortion and with no long-range magnetic order down to 4.2 K [5].

In 1972, Yoshimura et al. [7] reported that SrLaMnWO_6 was cubic ($a = 8.034 \text{ \AA}$) and semiconductive; they also studied the temperature-dependent magnetic susceptibility from ~ 80 to 1200 K, and observed a ferrimagnetic transition at $T_N \sim 400$ K. More recently, the powder neutron diffraction (PND) structure and the magnetic properties of $A_2\text{MnWO}_6$ ($A = \text{Ca}, \text{Sr}, \text{Ba}$) double perovskites have been reported [3,8–10]. The

*Corresponding author. Fax: +732 445 5312.

E-mail address: martha@rutchem.rutgers.edu (M. Greenblatt).

$A_2B'B''O_6$ double perovskites are generally described as cubic ($Fm\bar{3}m$), or tetragonal ($I4/m$) or monoclinic ($P2_1/n$) [3]. However, Azad et al. [9] reported that Sr_2MnWO_6 is tetragonal with space group $P4_2/n$, which is uncommon for double perovskites; they also observed a magnetic transition at ~ 45 K, which was not confirmed by the PND data [3]. In contrast, Muñoz et al. [3] argued that monoclinic $P2_1/n$ describes the symmetry of Sr_2MnWO_6 better than $P4_2/n$; and they observed magnetic reflections only below 15 K.

In this work, we studied the structure and magnetic properties of solid solution $Sr_{2-x}La_xMnWO_6$ ($0 \leq x \leq 1$), with the objective to resolve some of the controversies discussed above, and to evaluate the effect of La substitution (electron doping) on the magnetic properties. We also attempted to measure the transport properties, however, the room temperature resistivities of all compositions are larger than the limit of the measuring equipment (> 20 M Ω)—out of the range of interest for semiconductors. Attempts to synthesize $CaLaMnWO_6$ resulted in a mixture of a double perovskite and La_2O_3 impurity, while that of the $BaLaMnWO_6$ analog yielded a paramagnetic cation-deficient perovskite-related hexagonal phase, $Ba_2La_2MnW_2O_{12}$ (S.G. $R\bar{3}m$). Results of $Ba_2La_2MnW_2O_{12}$ will be published elsewhere [11].

2. Experimental

2.1. Synthesis

$Sr_{2-x}La_xMnWO_6$ ($x = 0, 0.5, 0.75, 0.9, 1.0$) were prepared by conventional solid-state reaction under 1% H_2/Ar flow. All the starting materials, $SrCO_3$ (99.99%, Alfa), La_2O_3 (99.99%, Alfa), Mn_2O_3 (99.99%, Alfa), WO_3 (99.99%, Alfa) were preheated and the purity of each was assured by powder X-ray diffraction (PXD). Stoichiometric mixtures of the starting reagents were ground, palletized and fired at 500 °C for 6 h, then at 1100 °C for 12 h, followed by heating at higher temperatures dependent on x . The window of the final firing temperature is quite narrow, $\pm 20(5)$ °C, and if not optimized, can result in the formation of $SrWO_4$ impurity. The final treatment is as follows: for $x = 0$, heat at 1150 °C for 36 h; while for $x = 0.5, 0.75$ and 0.9 , at 1180 °C for 48 h; and for $x = 1$, at 1200 °C for 144 h. To eliminate the presence of impurity phases, several intermediate grindings are required. The discrimination of MnO impurity in the $x = 0.75$ and 0.9 samples was possible only by Le Bail refinements, because the Bragg peaks of MnO and those of the double perovskites of $x = 0.75$ and 0.9 almost overlap. From the scale of intensity, we estimated ~ 0.5 % MnO impurity in both samples.

2.2. Powder X-ray diffraction analysis

PXD patterns for all compositions were recorded by a laboratory Bruker D8 Advanced X-ray diffractometer equipped with a solid-state detector. The useful 2θ range covered was 15–120° with a step size of 0.02°. Peak searching and indexing of the powder patterns were carried out with the XFIT [12] and TREOR90 [13] programs; the indexing and crystal symmetry were confirmed with the CHECKCELL program [14]. Le Bail fitting and structure refinements were carried out with the Jana2000 program [15]. In the profile refinements, the peak shape was simulated by a pseudo-Voigt function and the background was fitted with Legendre polynomial function. Since the structure model for $SrLaMnWO_6$ could not be confirmed by PXD analysis, high-resolution PND data were collected.

2.3. Powder neutron diffraction

PND data for $SrLaMnWO_6$ were collected with the high-resolution BT-1 32 detector powder neutron diffractometer at the NIST Center for Neutron Research. The sample was sealed in a vanadium container inside a dry He-filled glove box. A closed-cycle He refrigerator was used for temperature control. A Cu (311) monochromator with 90° take-off angle, $\lambda = 1.54030$ Å, and in-pile collimation of 15 min of arc were used. Data were collected over the range of 3–168° 2θ with step length of 0.05°. The instrument is described in the NCNR website (<http://www.ncnr.nist.gov/>). Structure refinements were performed using the FULLPROF program [16].

2.4. X-ray absorption spectroscopy (XAS)

The transition metal XAS measurements of Sr_2MnWO_6 and $SrLaMnWO_6$ were performed on beam lines X-19A and X18B, at the Brookhaven National Synchrotron Light Source, which, respectively, have double crystal and channel cut Si(111) monochromators. Both fluorescence and transmission mode measurements were made. The relative energies between various spectra were determined using a simultaneous standard and in general, the relative accuracy of the energy is about ± 0.1 eV. All spectra were normalized to unity step in the absorption coefficient from well below to well above the edge.

2.5. Magnetic measurements

Temperature-dependent magnetic susceptibility, χ , measurements were made with a Quantum Design MPMS-XL SQUID magnetometer. The samples were cooled to 5 K, then a magnetic field was applied and data were collected while heating from 5 to 385 or 750 K

(zero-field-cooled—ZFC) followed by re-cooling to 5 K (field-cooled—FC). The field-dependent magnetization measurements were performed with an applied field (H), $-5\text{ T} < H < 5\text{ T}$.

3. Results and discussion

3.1. Crystallographic structure

Fig. 1 shows the expanded PXD patterns between 32° and 59° of all the studied compositions. Close examination of the weak Bragg peaks (marked with dashed lines) suggests that the peak intensities decrease with increasing La concentration until they disappear at $x \sim 0.9$, typical fingerprint of symmetry-breaking. Hence, $0.75 < x < 0.9$ is considered as the boundary where the phase transition occurs.

The Bragg peaks of $\text{Sr}_{2-x}\text{La}_x\text{MnWO}_6$, $x = 0, 0.5, 0.75$, were indexed with $\sim \sqrt{2}a_p \times \sqrt{2}a_p \times 2a_p$ unit cells (a_p is the original perovskite cell parameter) and the structures were refined in the monoclinic $P2_1/n$ space group. The fit of the observed and calculated PXD profiles for the three compounds is shown in Fig. 2. The refined unit cell constants and the coordination parameters are given in Tables 1 and 2, respectively. In the refinement, the thermal factors of the oxygen atoms were constrained to be equal due to the large correlations with the occupancy. The refinement indicates that for $x = 0$ and 0.75 , the Mn and W atoms are completely ordered on the B -sites; for $x = 0.5$, a 3.0(3)% Mn/W antisite mixing is found. The X-ray crystallographic data of Sr_2MnWO_6 are basically consistent with that determined from PND by Muñoz et al. [3].

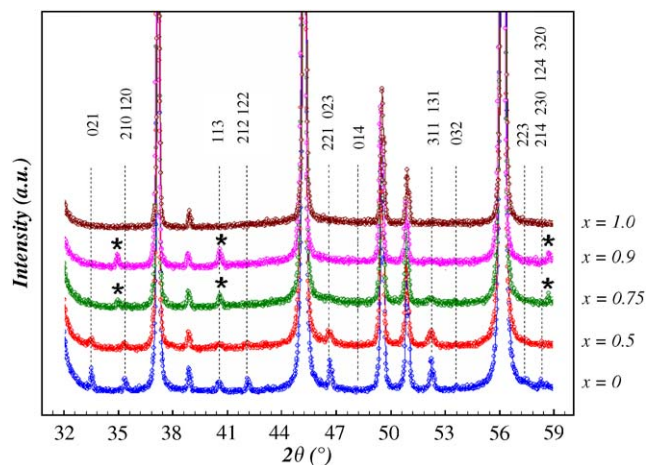


Fig. 1. Expanded PXD patterns for $\text{Sr}_{2-x}\text{La}_x\text{MnWO}_6$ ($0 \leq x \leq 1$) showing the evolution of weak peaks (between 32° and 59°) with La substitution. The index of peaks, which are absent for $x \geq 0.9$ are highlighted by dashed lines; peaks due to the MnO impurity are marked with asterisk.

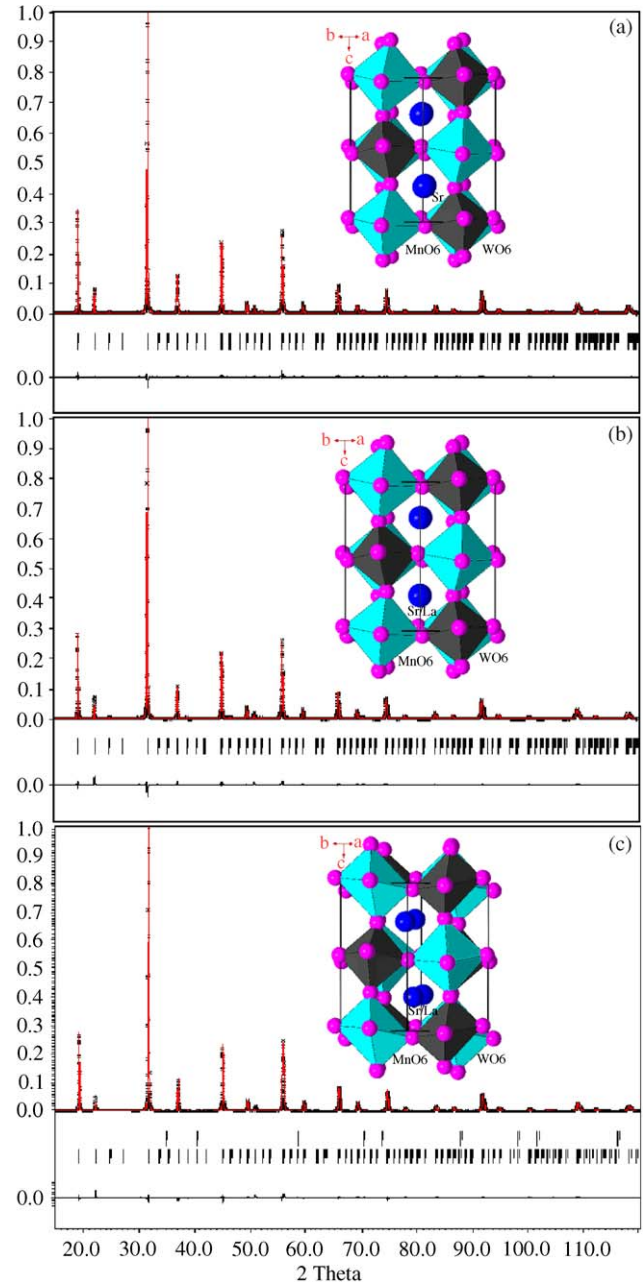


Fig. 2. Observed and calculated profiles of (a) Sr_2MnWO_6 , (b) $\text{Sr}_{1.5}\text{La}_{0.5}\text{MnWO}_6$ and (c) $\text{Sr}_{1.25}\text{La}_{0.75}\text{MnWO}_6$. Experimental points are shown by crosses and the calculated profile by solid line. The bottom curve is the difference pattern and the small bars indicate the angular positions of the allowed Bragg reflections. Insets of (a), (b) and (c) are the unit cell diagrams of each compound with MnO_6 and WO_6 in octahedral representation.

For SrLaMnWO_6 , the PXD patterns were initially indexed in cubic symmetry ($Fm\bar{3}m$) with $a \approx 8.02 \text{ \AA}$, which seemed in good agreement with that previously reported [7]. However, Rietveld analysis of the PXD data in the $Fm\bar{3}m$ model resulted in negative thermal parameters of the B -site cations and large residual electron density on the W position, suggesting a poor

Table 1
Powder X-ray crystallographic data for $\text{Sr}_{2-x}\text{La}_x\text{MnWO}_6$ ($x = 0, 0.5$ and 0.75)

	$x = 0$	$x = 0.5$	$x = 0.75$
Space group	$P2_1/n$	$P2_1/n$	$P2_1/n$
<i>Cell constants</i>			
a (Å)	5.6805(1)	5.6814(1)	5.6772(12)
b (Å)	5.6721(1)	5.6763(1)	5.6778(11)
c (Å)	8.0197(2)	8.0223(2)	8.0313(12)
β (°)	89.927(3)	89.964(9)	89.97(3)
V (cm ³)	258.40(1)	258.71(1)	258.88(8)
<i>Reliability factors</i>			
R_p	4.75	5.75	6.06
R_{wp}	6.52	8.43	9.73
R_E	4.21	4.55	4.67
GOF	1.55	1.85	2.08

Table 2
Atomic coordination parameters from Rietveld refinement of X-ray powder pattern at room temperature for $\text{Sr}_{2-x}\text{La}_x\text{MnWO}_6$ ($x = 0, 0.5$ and 0.75)

Atoms		0	0.5	0.75
Sr/La	x	0.9913(11)	0.9798(19)	0.9801(12)
	y	0.0198(3)	0.0165(6)	0.007(1)
	z	0.2551(8)	0.2611(16)	0.262(5)
	U_{iso} (Å ²)	0.0028(3)	0.0038(5)	0.0098(8)
Mn			($\frac{1}{2}$ 0 0)	
	B (Å ²)	0.0035(4)	0.0040(5)	0.0065(5)
W			($\frac{1}{2}$ 0 $\frac{1}{2}$)	
	B (Å ²)	0.0017(2)	0.0032(4)	0.0081(6)
O1	x	0.5563(15)	0.5527(10)	0.546(5)
	y	0.003(2)	0.002(5)	0.003(8)
	z	-0.263(6)	-0.2639(7)	-0.2640(6)
	U_{iso} (Å ²)	0.0104(11)	0.0096(12)	0.0179(14)
O2	x	0.726(8)	0.755(10)	0.763(14)
	y	0.299(8)	0.277(9)	0.268(13)
	z	0.024(6)	0.022(12)	-0.017(19)
	U_{iso} (Å ²)	0.0104(11)	0.0096(12)	0.0179(14)
O3	x	0.211(7)	0.206(8)	0.211(10)
	y	0.240(7)	0.233(9)	0.241(7)
	z	-0.028(6)	-0.031(10)	0.039(13)
	U_{iso} (Å ²)	0.0104(11)	0.0096(12)	0.0179(14)

The Sr/La ratio was fixed according to the nominal composition, ~ 3.0 (3)% Mn/W antisite mixing was refined in the $x = 0.5$ sample.

structure model. This motivated the high-resolution PND study to determine the correct crystal symmetry of this phase.

Similar to the PXD data, the PND structure refinements with the $Fm\bar{3}m$ model resulted in poor reliability factors ($R_p = 8.36\%$, $wR_p = 13.2\%$), negative thermal factors for the B -site cations, and a large thermal factor for the oxygen ($B_{iso} = 6.62 \text{ \AA}^2$). For systems with large

thermal factors, higher-order atomic displacement parameters (ADPs) may carry useful information and deserve special attention [17]. However, the thermal factors for Mn and W remained negative, even when the ADPs for oxygen were refined by the Jana2000 program. Further doubt on the $Fm\bar{3}m$ model was cast by the anomalously high value (0.593) of the global instability parameter, calculated with the SPUDS program [18].

Re-evaluation of the indexing of the PXD peaks in Fig. 1 revealed that the 021, 210, 120, 113, 212, 122, 221, 023, etc. Bragg peaks observed in $P2_1/n$ symmetry for $x \leq 0.75$ are absent for $x = 1$. These indices could be classified for either F -centered ($h+k, k+l, h+l: 2n+1$) or I -centered ($h+k+l: 2n+1$) systematic extinctions. No super-lattice reflections were observed, and all the observed reflections in SrLaMnWO_6 can be indexed in the $Fm\bar{3}m$ model with a $2a_p \times 2a_p \times 2a_p$ unit cell. According to the Glazer's tilting systems with 1:1 B -site cation ordering [19], only space groups with I -centered symmetry, and with $\sim \sqrt{2}a_p \times \sqrt{2}a_p \times 2a_p$ unit cell will *not* generate redundant reflections; only three space groups, $I4/m$, $I2/m$ and $I\bar{1}$ satisfy these conditions.

When questions arise about the correctness of crystal symmetry associated with a phase transition, Landau theory [20,21] may provide the answer. One of the main advantages of the Landau theory is that it provides symmetry constraints for symmetry-breaking processes. From Fig. 1, it is evident that SrLaMnWO_6 has higher symmetry (fewer observed Bragg peaks) than monoclinic, thus $I\bar{1}$ can be excluded. According to group-theory analysis [22], the transition from tetragonal $I4/m$ to monoclinic $P2_1/n$ is a first-order transition, while the transition from $I2/m$ to $P2_1/n$ can be continuous (second order). The variation of the refined unit cell parameters, (b/a) as a function of La content (x) in Fig. 3 shows a sharp onset around $0.75 < x < 0.9$,

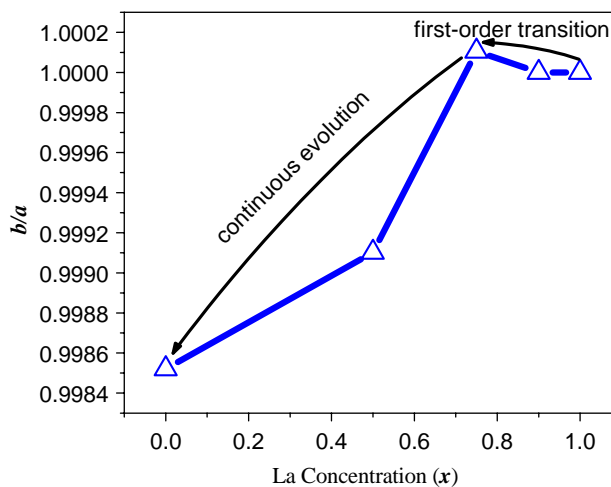


Fig. 3. Variation of the unit cell parameters with x for $\text{Sr}_{2-x}\text{La}_x\text{MnWO}_6$ ($0 \leq x \leq 1$).

Table 3

Atomic coordination parameters and anisotropic thermal parameters ($\times 10^{-3} \text{ \AA}^2$) for SrLaMnWO₆ obtained from the Rietveld refinement of the neutron powder diffraction pattern with $\lambda = 1.5403 \text{ \AA}$

Atoms	Wyck.	<i>x</i>	<i>y</i>	<i>z</i>	<i>U</i> ₁₁	<i>U</i> ₂₂	<i>U</i> ₃₃	<i>U</i> ₁₂	<i>U</i> ₁₃	<i>U</i> ₂₃
Sr/La	4 <i>d</i>	0	$\frac{1}{2}$	$\frac{1}{4}$	36(2)	36(2)	36(2)	0	0	0
Mn	2 <i>a</i>	0	0	0	21(1)	21(1)	5(2)	0	0	0
W	2 <i>b</i>	0	0	$\frac{1}{2}$	7(4)	7(4)	22(8)	0	0	0
O1	4 <i>e</i>	0	0	0.2632(2)	69(2)	69(2)	4(4)	0	0	0
O2	8 <i>h</i>	0.2216(4)	0.3044(4)	0	9(2)	3(1)	85(3)	2(1)	0	0

$R_p = 4.70\%$, $R_{wp} = 5.74\%$, $R_E = 5.12\%$, $\chi^2 = 1.26$.

Space group *I4/m*, $a = 5.6741(1) \text{ \AA}$, $c = 8.0253(2) \text{ \AA}$.

which suggests a discontinuous (first-order) transition from SrLaMnWO₆ to Sr₂MnWO₆. Accordingly, the correct space group for SrLaMnWO₆ is expected to be *I4/m*, which is confirmed by the structure analysis below.

For the *I4/m* model, the cell and atomic coordinate parameters were transformed from the *Fm* $\bar{3}$ *m* model. The refinements indicated that Mn and W are fully ordered at the 2*a* and 2*b* positions. An unconstrained refinement of oxygen occupancies showed no oxygen deficiency for SrLaMnWO₆. The final refinement with anisotropic thermal parameters proceeded smoothly and converged at $R_p = 4.70\%$, $wR_p = 5.74\%$, $\chi^2 = 1.26$. The refined atomic parameters are summarized in Table 3 and the observed and calculated PND profiles for SrLaMnWO₆ are shown in Fig. 4. The schematic unit cell with polyhedral representation is shown in the inset of Fig. 4, with the (*a*⁰*a*⁰*c*⁻) tilting (Glazer's notation) [19] of MnO₆ and WO₆ octahedra.

Although PND data in general yield more accurate bond distances and angles than PXD data, the PXD structure for $x = 1$ was also refined in *I4/m* to compare the structural parameters with all the other Sr_{2-*x*}La_{*x*}MnWO₆ phases with only PXD structural results. The refined bond distances and angles together with bond valence sum results of Mn and W, and tilting angles of the (Mn/W)O₆ octahedra are collected in Table 4 for all the phases studied. The Mn/W–O bond distances are in good agreement with those observed before [3,8–10]. Comparison of the PXD data for the Mn/W–O inter-atomic distances with increasing *x* indicates changes that are within the experimental error (Table 4).

A remarkable structural feature of Sr_{2-*x*}La_{*x*}MnWO₆ is the evolution of the Mn–O–W bond angles (ϕ), which reflect the structural distortion from ideal cubic perovskite, and, which have important implications for the interpretation of the magnetic data (vide infra). The octahedral tilting angle (φ) of the MnO₆ and WO₆ octahedra is defined as $\varphi = (180 - \bar{\varphi})/2$ [3]. As calculated, and regardless that the title compounds belong in different tilting systems, i.e., different space groups, φ

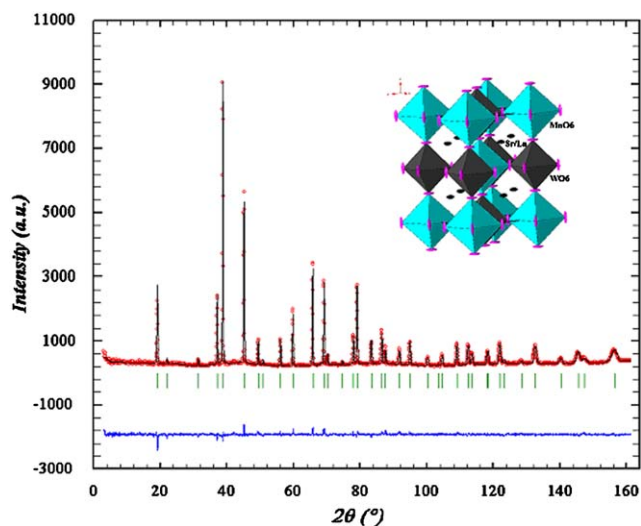


Fig. 4. Rietveld refinement of SrLaMnWO₆ neutron powder diffraction data. Experimental points are shown by circles and the calculated profile by solid line. The bottom curve is the difference pattern and the small bars indicate the angular positions of the allowed Bragg reflections. Inset: unit cell diagram for SrLaMnWO₆; atoms are drawn with ellipsoid representation.

stepwise decreases from 9.2° for Sr₂MnWO₆ to 6.8° for SrLaMnWO₆ (Table 4).

3.2. X-ray absorption spectroscopy analysis

Fig. 5 shows the Mn–K edges of Sr₂MnWO₆ and SrLaMnWO₆ along with several standards. The Mn–K main features involve transitions into *p*-symmetry states above the Fermi energy. The chemical shift of the onset of the edge is typically used as a valence-state indicator; however, this determination is complicated by the details of spectral-feature splittings at the edge, which can vary depending on the local symmetry and hybridization effects. In the strongly hybridized MnO, e.g., a broad shoulder *a*-feature lies at a lower energy than split *b*-feature peaks. Comparing the double perovskite spectra to that of Mn²⁺O and LaMn³⁺O₃, one can infer a basically Mn²⁺ state for both

Table 4
Interatomic Mn–O and W–O bond distances, bond valence summation (BVS) and octahedral tilting angles (φ) for $\text{Sr}_{2-x}\text{La}_x\text{MnWO}_6$ ($0 \leq x \leq 1$)

x	0	0.5	0.75	0.9	1.0	1.0 ^a
Mn–O1 (Å)	2.13(5)	2.138(6)	2.14(1)	2.13(1)	2.14(2)	2.112(2)
Mn–O2 (Å)	2.14(5)	2.15(5)	2.14(8)	2.17(5)	2.16(2)	2.136(2)
Mn–O3 (Å)	2.15(4)	2.15(5)	2.16(5)			
Average	2.14(1)	2.15(1)	2.15(2)	2.15(2)	2.15(1)	2.128(2)
BVS	2.1	2.1	2.1	2.1	2.1	2.1
W–O1 (Å)	1.93(5)	1.918(6)	1.91(1)	1.89(1)	1.88(2)	1.900(2)
W–O2 (Å)	1.94(5)	1.89(5)	1.89(7)	1.93(5)	1.95(2)	1.931(2)
W–O3 (Å)	1.91(4)	1.93(5)	1.92(5)			
Average	1.93(2)	1.92(2)	1.91(2)	1.92(2)	1.92(4)	1.921(2)
BVS	5.7	5.0	5.0	5.0	5.0	4.9
\angle Mn–O1–W (°)	161.8(3)	162.9(3)	165.1(3)	180	180	180
\angle Mn–O2–W (°)	160.1(3)	168.7(3)	172.1(4)	156.0(2)	159.5(9)	161.2(1)
\angle Mn–O3–W (°)	163.0(2)	160.2(3)	159.2(3)			
φ (°)	9.2	8.0	7.3	8.0	6.8	6.3

^aNeutron powder diffraction data.

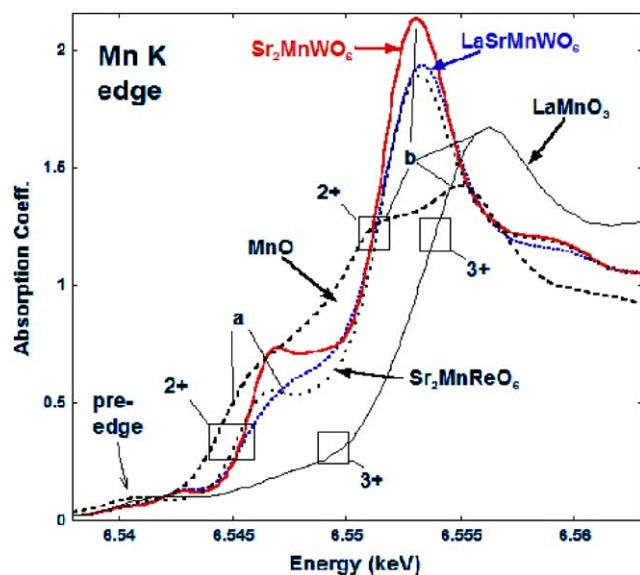


Fig. 5. XAS spectrum of Mn–K edge of Sr_2MnWO_6 and SrLaMnWO_6 .

compounds. Boxes in Fig. 5 indicate the nominal energy ranges through which Mn^{2+} - and Mn^{3+} -type spectra would pass for both the a and b features. This Mn^{2+} characterization is similar to that we determined previously [4] for $\text{Sr}_2\text{MnReO}_6$, the spectrum for which is also shown in Fig. 5. It is worth noting that the a and b features in the $x = 1$ spectrum are substantially broadened relative to those in the $x = 0$ spectrum. One source of this broadening is the disordered La/Sr sites creating a distribution of local environments. The local electron density increase accompanying the La substitution should also provide a dampening/relaxing mechanism

for the sharp ionic-like a and b transitions observed in the $x = 0$ compound. The changes involved in the Mn–K edge spectra could also be related to shifts in the degree of Mn–O covalency upon La substitution.

The L_3 edges of transition metal compounds are dominated by an intense “white line” (WL) feature involving transitions into empty d final states. The W– L_3 edges for Sr_2MnWO_6 and SrLaMnWO_6 , along with some standard compounds, are shown in Fig. 6b. The WL features of the double perovskite spectra are distinctly bimodal with the unresolved A and B features associated with transitions into the empty 6-fold degenerate t_{2g} and 4-fold e_g final $5d$ states, respectively. The A – B feature splitting reflects the ligand field splitting of the $5d$ -orbitals and is ~ 3.5 – 3.9 eV in these perovskites. Comparison of the perovskite spectra in Fig. 6b reveals a modest decrease in the A – B feature (ligand field) peak-to-peak splitting from 3.9 eV for Sr_2MnWO_6 to 3.5 eV for SrLaMnWO_6 . The La/Sr disorder could contribute to a local distribution-induced ligand field broadening. The excess local electron density, due to the La^{3+} for Sr^{2+} substitution, could also contribute a local screening/dampening of the W-site ligand field.

Referring to the W– L_3 standard compound spectra in Fig. 6b, the chemical shift of the center of the WL to higher energy, with increasing W-valence, can be seen in the W^0 – W^{4+} – O_2 – W^{6+} – O_3 sequence of spectra. The chemical shift of the Sr_2MnWO_6 spectrum would appear to be comparable to that of W^{6+} – O_3 ; however, the bimodal-perovskite A – B WL-feature makes a quantitative estimate difficult. Careful comparison of the high- and low-energy sides of the perovskite spectra does, however, evidence a small chemical shift to lower energy for the SrLaMnWO_6 spectrum. Thus there is evidence for a W-site valence decrease (albeit apparently modest) in response to the La substitution.

The only-modest W– L_3 spectral change between Sr_2MnWO_6 and LaSrMnWO_6 motivates their consideration in the context of other $5d$ perovskite-based transition metal (T) L_3 spectral results. In Fig. 6a, the $T = \text{Ta}$ and Re T – L_3 edges for two octahedrally coordinated, perovskite-based oxides are shown on a 22 eV-wide energy scale similar to that in Fig. 6b. Here the Re compounds were prepared as described in Ref. [4]. The Ta compound was prepared at Rutgers and characterized after the methods described in Refs. [24,25]. The Ta and Re WL features, in Fig. 6a, display bimodal A and B features similar to those in Fig. 6b. The smaller A – B feature splitting indicates a smaller ligand field splitting of ~ 2.5 eV for these Re/Ta compounds. One should note that the t_{2g} -final-state-related A -feature loses intensity relative to the e_g -final-state-related B -feature between the Ta^{5+} - d^0 and Re^{6+} - d^1 spectra. This is consistent with the decrease in $5d$ - t_{2g} hole states in the latter. Moreover, the A -feature being

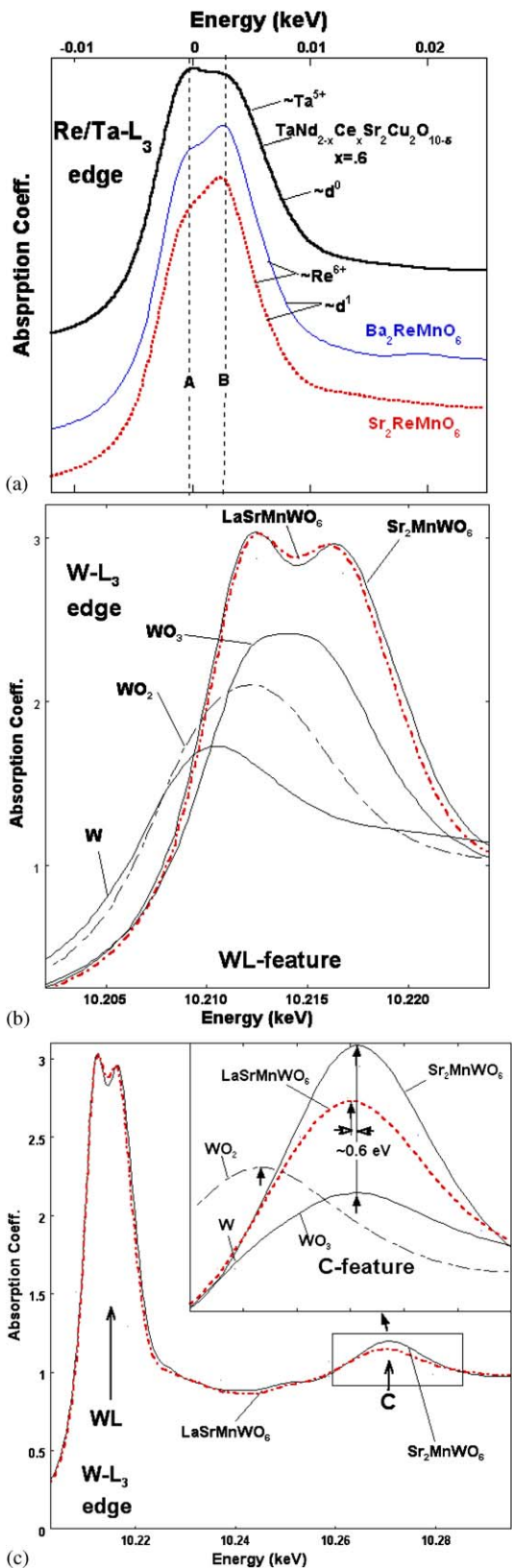


Fig. 6. XAS spectra of W-L₃ edge of Sr₂MnWO₆ and SrLaMnWO₆.

somewhat more intense than the *B*-feature in the Sr₂MnWO₆ spectrum in Fig. 6b would appear to fit consistently into this pattern with its W⁶⁺-*d*⁰ assign-

ment. Extending this trend, the *A*-feature of the SrLaMnWO₆ spectrum would be expected to have a significantly lower intensity than is observed, to be consistent with the formally W⁵⁺-*d*¹ assignment. The suggestion is made here that the La substitution may have induced a local covalency change as opposed to *d*-orbital charge loss. However, the possibility of an unexpected insensitivity of the XAS technique to the W⁶⁺-W⁵⁺ change must also be acknowledged. This open issue is important to note since it has bearing both on the properties of these W-compounds and on the XAS technique.

In Fig. 6c, an expanded view of the XAS fine structure oscillations above the W-L₃ edge is shown. The *C*-feature, indicated in the figure, can be viewed as a continuum resonance caused by the O-ligand-shell or equivalently as the first extended X-ray absorption fine structure oscillation enhanced by multiple scattering effects (see Ref. [4]). In either case, the energy of the *C*-feature relative to the edge has been shown to reflect the average radius of the O-ligand-shell. As illustrated, the shift of the *C*-feature peak to higher energy between the WO₂ to WO₃ spectra, in the inset of Fig. 6c, reflects the contraction of the O-shell in the higher-valence compound. The energies of the *C*-features of WO₃ and the Sr₂MnWO₆ are comparable, and consistent with their ~W⁶⁺ state. The *C*-feature energy in the SrLaMnWO₆ spectrum is shifted down in energy, again quite slightly, suggesting a small expansion of the W-O bond length in response to the La substitution. This observation would tend to support the interpretation that the La-substitution-induced W-valence change is only modest. However, as noted above this question must at present remain open.

3.3. Magnetic properties

The temperature dependence of the magnetic susceptibility (χ) and the inverse magnetic susceptibility ($1/\chi$) for Sr₂MnWO₆ are shown in Fig. 7. The profile is typical of paramagnetic-to-antiferromagnetic (AFM) transition at ~15 K. A fit to a simple Curie-Weiss (CW) law, $\chi = C/(T-\theta)$, for data between 200 and 385 K yields $C = 4.7$ emu K/mol ($\mu_{\text{eff}}^{\text{obs}} = 6.13 \mu_{\text{B}}$) and a Weiss constant (θ) of -82.0 K. These results are comparable to those previously reported ($T_{\text{N}} \sim 13$ K) [9]; however, we did not observe the divergence of the FC and ZFC data and a magnetic transition at ~45 K reported by Azad et al. [9]. Our results are in good agreement with the thermal evolution of the PND data of Muñoz et al. [3]. Thus the $x = 0$ compound in this series is an insulating AFM material. The value of $\theta = -82.0$ K for a compound which orders at $T_{\text{N}} \sim 15$ K does however suggest possible Mn-O covalency effects.

La substitution in Sr_{2-x}La_xMnWO₆ should induce, at least on the local scale, some admixture of a W⁵⁺ (*d*¹)

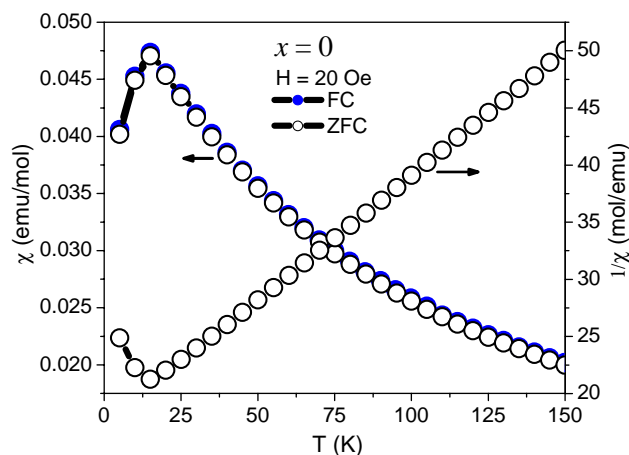


Fig. 7. Temperature-dependent molar susceptibility and its inverse for Sr_2MnWO_6 .

character into the W^{6+} (d^0), $x = 0$ compound. The W-L_3 XAS results (discussed above) support this expectation, although, they also suggest that the W^{5+} admixture is smaller than formally expected. A W^{5+} (d^1) XAS standard would help on this issue. In the $\text{Sr}_2\text{MoFeO}_6$ system, the Mo^{5+} sites have been discussed not as local moment sites but as Pauli-paramagnetic sites whose exchange polarization supports a ferromagnetic (FM) Fe–Fe interaction [23]. Alternatively, this can be viewed as a ferrimagnetic Fe–Mo–Fe coupling with the caveat that the Mo sites lack a full local moment. In $\text{Sr}_{2-x}\text{La}_x\text{MnWO}_6$ the induced W^{5+} (d^1) character might be expected to play a role similar to the Mo^{5+} (d^1) sites in the $\text{Sr}_2\text{FeMoO}_6$ system; namely to mediate effective local Mn–Mn FM interactions. The broader, lower density of states of the W-5d band, compared to the Mo-4d case, should make this W^{5+} (d^1) mediation substantially weaker than in the Mo system. Moreover, because the $\text{Sr}^{2+}/\text{La}^{3+}$ sites are disordered, there will be a distribution of local W^{5+} -site character, and of the effective Mn–Mn FM interactions. With these points in mind, we will discuss the magnetic results on the $\text{Sr}_{2-x}\text{La}_x\text{MnWO}_6$ system.

The temperature-dependent magnetic susceptibilities and their inverse for $\text{Sr}_{1.5}\text{La}_{0.5}\text{MnWO}_6$, $\text{Sr}_{1.25}\text{La}_{0.75}\text{MnWO}_6$ and SrLaMnWO_6 are shown in Figs. 8a–f. The calculated Weiss constants (θ) in Table 5 are negative, indicating that the predominant magnetic interactions are AFM, with θ decreasing with increasing x , dramatically so for samples $x \geq 0.5$ (Table 5). The values of the observed effective magnetic moments ($\mu_{\text{eff}}^{\text{obs}}$) are in fairly good agreement with those calculated (μ^{cal}) assuming spin-only interactions. Here it should be noted however, that a formal fraction x of W^{5+} (d^1) has been included in the μ^{cal} calculation. In view of our comments above, about the probable lack of local moment at the W sites, the Mn-only $\mu^{\text{cal}} = 5.92 \mu_{\text{B}}$ effective moment (at

$x = 0$) is in very good agreement with the $\mu_{\text{eff}}^{\text{obs}}$ values of the $x = 0.5, 0.75$ and 1.0 compounds, indicating that W is not contributing to the moment.

The low-field $x = 0, 0.5$ and 0.75 magnetic results in Figs. 8a and c, respectively, evidence the development of a weak FM moment in the 50–60 K temperature range. This observation, along with the AFM-like θ values (40–45 K, Table 5) is consistent with the onset of a canted-AFM phase in the 50–60 K range for these materials. Specifically, the weak-FM moment is coupled to, and grows with the AFM order parameter as it develops below the transition temperature. The canted FM component of the order would almost certainly vary in magnitude locally depending on the local La/Sr coordination. The pronounced FC vs. ZFC effect in the $x = 0.5$ material, which vanishes approaching the order in temperature from below, is worth noting (Fig. 8a). In the ZFC case, at low temperature, the AFM domains have developed randomly and their randomly canted moments are not free to respond to the external field. Upon increasing temperature, the weakening order frees more AFM domains to reorient their canted moments along the field, hence the increase in χ . Finally, as $T \rightarrow T_{\text{N}}$ from below, the decreasing AFM order parameter pulls down the canted moment and the χ decreases. In the FC case, the AFM domains grew with their canting direction preferentially along the field direction, the χ is larger in the ordered state, and the domain-related χ maximum is weaker.

An inhomogeneous distribution of magnetic effects is to be expected in these materials on a number of length scales. As indicated above, the effective canted moment distribution of the AFM domains should be field (H), temperature (T) and H – T -history dependent. On a local scale, high La concentration could create local FM Mn correlations into a large cluster moment moiety, whereas Sr-rich regions should have local AFM correlations reminiscent of the $x = 0$ material. Thus field-dependent and glassy magnetic effects can be anticipated in these materials. Referring to the $H = 500$ Oe susceptibility results (for the $x = 0.5$ material) in Fig. 8b, one notes that the field has essentially saturated out the low-field canted domain orientation effects evident in Fig. 8a. Moreover, the signature of the magnetic ordering has also been substantially reduced in the $H = 500$ Oe magnetic response. It would appear that local FM Mn–Mn correlated regions are capable of responding as large moments and that these moments dominate the higher field response. These moments would presumably be associated with high La correlation local environments.

The magnetic results for the $x = 0.75$ compound (Fig. 8c and d), as noted earlier, are qualitatively similar to those of the $x = 0.5$. The detailed magnetic response changes in the $x = 0.75$ material (relative to the $x = 0.5$) are: the low-field ($H = 20$ Oe) FC vs. ZFC anomalies in

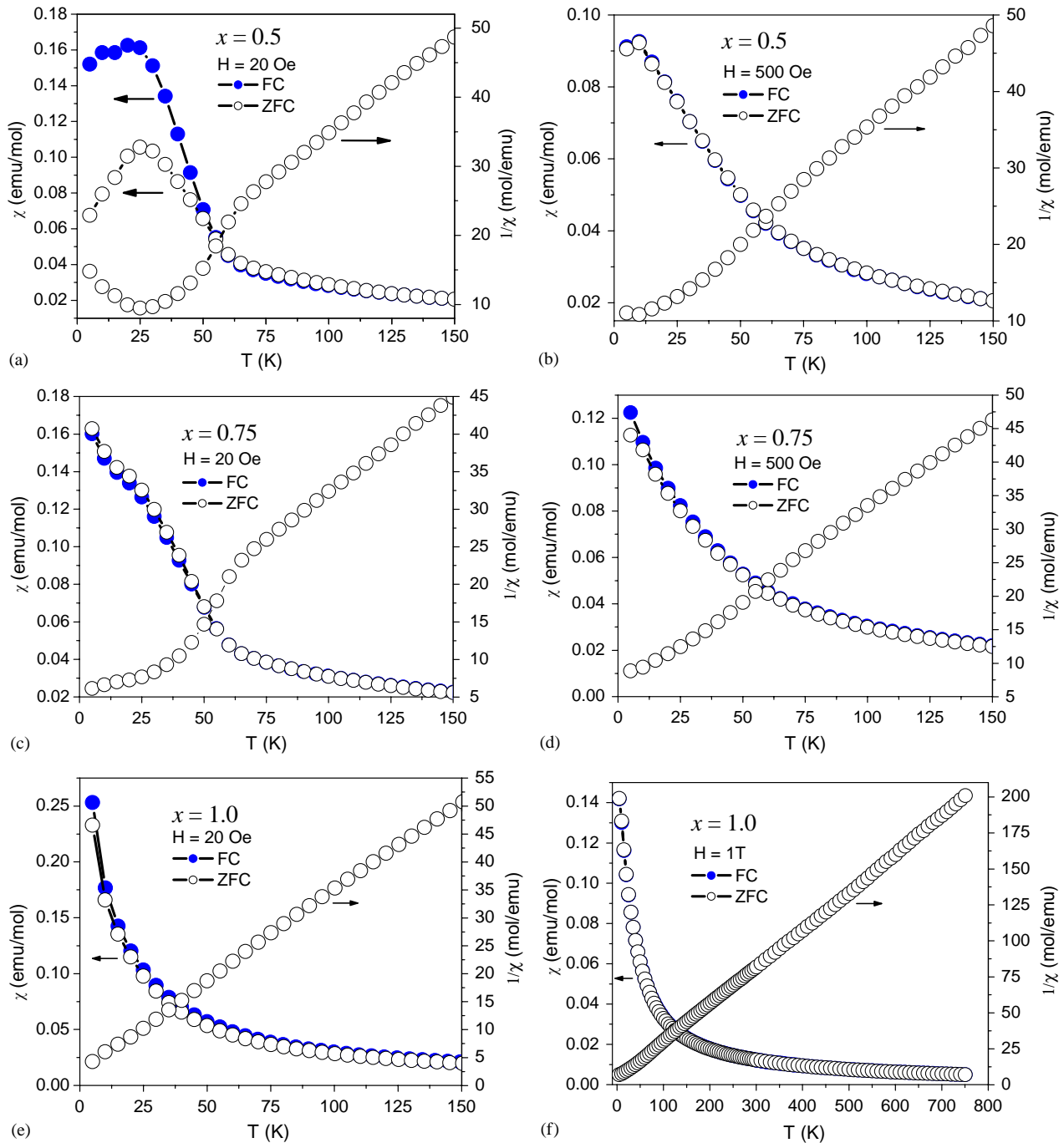


Fig. 8. Temperature-dependent molar susceptibility and its inverse for $\text{Sr}_{2-x}\text{La}_x\text{MnWO}_6$ ($0.5 \leq x \leq 1$).

Table 5
Curie constant, Curie temperature and effective magnetic moment ($\mu_{\text{eff}}^{\text{obs}}$) for $\text{Sr}_{2-x}\text{La}_x\text{MnWO}_6$ ($0 \leq x \leq 1$) obtained at 500 Oe

x	C	θ (K)	$\mu_{\text{eff}}^{\text{obs}}$ (μ_{B})	μ^{cal} (μ_{B})
0	4.7	-82.0	6.13	5.92
0.5	4.1	-44.7	5.73	6.02
0.75	4.1	-41.7	5.73	6.13
1.0	4.4	-39.5	5.93	6.16

the $T < 25$ K range are greatly reduced; the signatures of the canted-AF ordering in the 50–60 K range, are less distinct; and the higher-field (500 Oe) magnetic response is enhanced. All of these modifications are at least consistent with a higher concentration of formal W^{5+} sites creating local clusters of FM Mn–Mn domains, which respond with a large effective moment.

Turning to the $x = 1.0$ magnetic results (Fig. 8e and f), one notes that the anomalies, observed in the

50–60 K in the $x \leq 0.75$ materials, are not discernable to the naked eye. Thus there is no clear evidence for magnetic order in this material. Inspection of $d(\chi^{-1})/dT$ vs. T or χT vs. T plots (not shown) of the magnetic data reveals the vestiges of a change over in the 50–60 K range that is similar to that observed in the $x = 0.5$ and 0.75 materials. Recall that the clarity of the canted AFM transition (in the χ) decreased from $x = 0.5$ to 0.75 and from lower to higher field. Thus there is the possibility that the canted AFM state still occurs for $x = 1.0$, but with an extremely subtle χ -signature. The fact that the θ value at $x = 1.0$ is also only somewhat reduced, from that in the lower x materials (Table 5), is also suggestive of persistent AFM correlations. However, the presence of canted AFM order in the $x = 1.0$ material must remain open. Clearly, magnetic neutron scattering data would be decisive here. The fact that the $x = 1.0$ compound does possess a low-temperature moment which responds in modest fields can however be asserted from the magnetization results below.

Fig. 9a shows the magnetic field (H) dependent magnetization, M , for all compositions obtained at 5 K. Here only the positive part of the entire hysteresis loop is shown so that the details of the data can be seen. The highest field linear approximations for all of the $M(H)$ plots are indicated by lines and the slope of these lines is referred to as the high field susceptibility, χ_{HF} . For the $x = 0$, $M(H)$ results, the high-field linear portion extrapolation falls slightly below the low-field data. This is typical of an AFM material where the AFM order parameter is being non-linearly destroyed in field and where an S-shaped magnetization curve is expected. This point is emphasized in Fig. 9a—inset where the magnetization divided by the field (M/H) is plotted for $x = 0.0$, and the AFM moment suppression at lower fields is displayed more clearly. For $x \geq 0.5$ the lower field $M(H)$ data curve downward from the high-field linear extrapolation (see Fig. 9a—main figure). This is typical of a moment contribution that can be partially saturated in field. This effect (and its contrast to the AFM effect) is underscored in Fig. 9a—inset where the M/H data for $x = 1.0$ are shown.

Subtracting a linear field response yields an estimate of the moment saturation behavior, below 5 T. Accordingly the quantity $\{M(H) - H\chi_{\text{HF}}\}$ is plotted for $x = 1.0$ in Fig. 9b and the M_{sat} (high field limit) is indicated in the figure. In inset of Fig. 9b the values of both M_{sat} and χ_{HF} are plotted vs. composition x (note that the as-defined M_{sat} would be negative and is not meaningful for the AFM $x = 0$ material). The magnitudes of the saturated magnetic moments, M_{sat} are very low, consistent with AFM underlying interactions in all compositions; however, the M_{sat} increases with La (or W^{5+}) concentration, which suggests that the canting moment and local FM contributions increase with increasing W^{5+} content. The steady increase of χ_{HF}

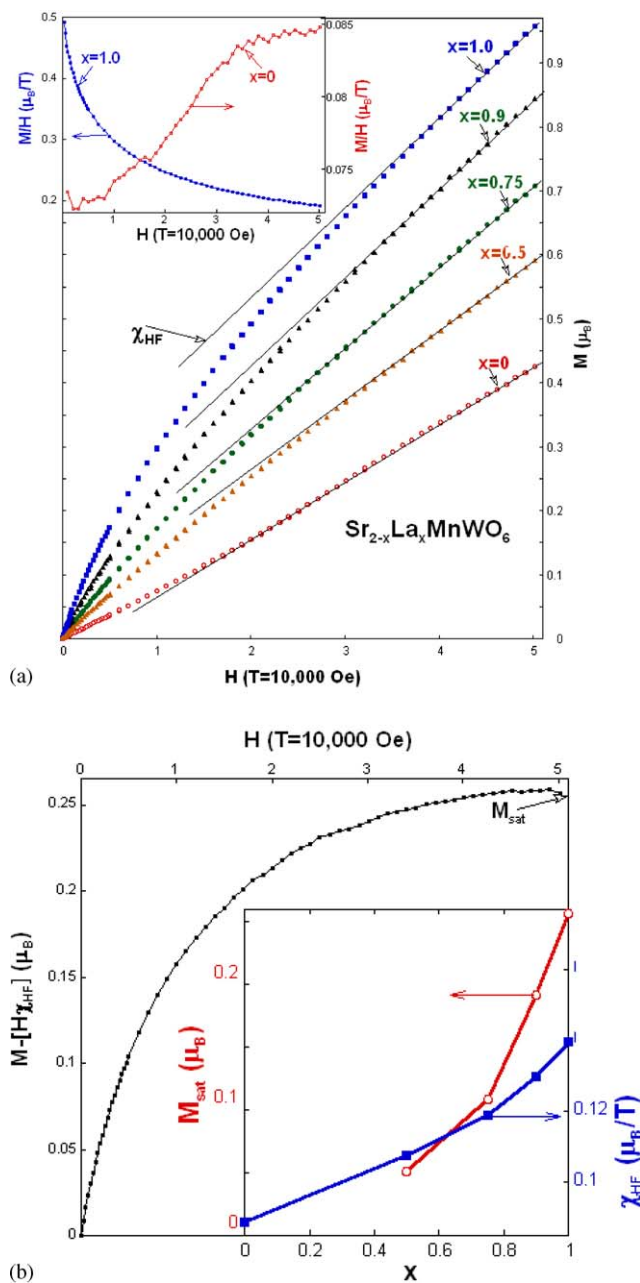


Fig. 9. (a) Main: The magnetic field (in Tesla $T = 10,000$ Oe) dependent molar magnetization, M , (in units of moment μ_B per formula unit) for $\text{Sr}_{2-x}\text{La}_x\text{MnWO}_6$ ($0 \leq x \leq 1$). The linear high-field slope of the magnetization χ_{HF} (the high field susceptibility) is also indicated. Inset: The magnetization divided by the field (in units of μ_B per T) is 28 plotted vs. field to underscore the different magnetic response in the AFM $x = 0$ and 1.0 material where FM correlations are also involved, (b) Main: The magnetization, minus the linear high-field component $\{M - H\chi_{\text{HF}}\}$ is plotted vs. field to illustrate the saturating component of the magnetization M_{sat} (also indicated in the figure) for the $x = 1.0$ material. Inset: The saturating component of the magnetization M_{sat} and the linear high field susceptibility χ_{HF} as a function of x for the $\text{Sr}_{2-x}\text{La}_x\text{MnWO}_6$ ($0 \leq x \leq 1$) system.

with x also indicates that the populations of smaller FM moment clusters, that will saturate at higher field, are also increasing.

4. Conclusion

The ordered double perovskite, $\text{Sr}_{2-x}\text{La}_x\text{MnWO}_6$ ($0 \leq x \leq 1$) solid solution was investigated. Powder X-ray and neutron diffraction structure analysis reveal that La substitution has pronounced influence on the crystal structure: for $x \leq 0.75$, the structure retains a monoclinic $P2_1/n$ space group with *B*-site ordering, while for $x = 1.0$, the structure is tetragonal $I4/m$. The phase boundary occurs at $\sim 0.75 < x < 0.9$. Increasing La substitution decreases the structural distortion from the ideal cubic perovskites. Magnetic measurements reveal that increasing La substitution introduces increasing FM interactions into the system with an apparent canted AFM ordering resulting. Local variations in the FM cluster moments make the AFM ordering increasingly difficult to observe in macroscopic magnetic measurements with the ordering of the $x = 1.0$, SrLaMnWO_6 material being uncertain.

Acknowledgments

The authors are grateful to Dr. M.V. Lobanov for helpful discussions and Dr. B. Toby of NIST for collecting the neutron data. This work was supported by the National Science Foundation—Solid State Chemistry Grant DMR-0233697.

References

- [1] K.-I. Kobayashi, T. Kimura, H. Sawada, K. Terakura, Y. Tokura, *Nature* 395 (1998) 677.
- [2] K.-I. Kobayashi, T. Kimura, Y. Tomioka, H. Sawada, K. Terakura, Y. Tokura, *Phys. Rev. B* 59 (1999) 11159.
- [3] A. Muñoz, J.A. Alonso, M.T. Casais, M.J. Martínez-Lope, M.T. Fernández-Díaz, *J. Phys.: Condens. Matter* 14 (2002) 8817.
- [4] G. Popov, M. Greenblatt, M. Croft, *Phys. Rev. B* 67 (2003) 024406.
- [5] E.I. Caspi, J.D. Jorgensen, M.V. Lobanov, M. Greenblatt, *Phys. Rev. B* 67 (2003) 13443.
- [6] S. Li, M. Greenblatt, *J. Alloys Compd.* 338 (2002) 121.
- [7] M. Yoshimura, K. Kamata, T. Nakamura, *Chem. Lett.* (1972) 737.
- [8] A.K. Azad, S.A. Ivanov, S.-G. Eriksson, J. Eriksen, H. Rundlöf, R. Mathieu, P. Svedlindh, *Mater. Res. Bull.* 36 (2001) 2215.
- [9] A.K. Azad, S.A. Ivanov, S.-G. Eriksson, H. Rundlöf, J. Eriksen, R. Mathieu, P. Svedlindh, *J. Magn. Magn. Mater.* 237 (2001) 124.
- [10] A.K. Azad, S.A. Ivanov, S.-G. Eriksson, J. Eriksen, H. Rundlöf, R. Mathieu, P. Svedlindh, *Mater. Res. Bull.* 36 (2001) 2485.
- [11] Q. Lin, M. Greenblatt, unpublished results.
- [12] R.W. Cheary, A.A. Coelho, *J. Appl. Crystallogr.* 25 (1992) 109.
- [13] P.-E. Werner, *Z. Kristallogr.* 1203 (1964) 75.
- [14] J. Laugier, B. Bochu, LMGP-Suite Suite of programs for the interpretation of X-ray experiments. URL: <http://www.inpg.fr/LMGP>.
- [15] V. Petricek, M. Dusek, Jana2000. The Crystallographic Computing System, Institute of Physics, Praha, Czech Republic, 2000.
- [16] J. Rodriguez-Carvajal, FULLPROF: a program for rietveld refinement and pattern matching analysis, Abstracts of the Satellite Meeting on Powder Diffraction of the XV Congress of the IUCr, Toulouse, France, 1990, p. 127.
- [17] W.F. Kuhs, *Acta Crystallogr. A* 48 (1992) 80.
- [18] M.W. Lufaso, P.M. Woodward, *Acta Crystallogr. B: Struct. Sci.* 57 (2001) 725.
- [19] P.M. Woodward, *Acta Crystallogr. B: Struct. Sci.* 53 (1997) 32.
- [20] L.D. Landau, E.M. Lifshitz, *Statistical Physics*, vol. 5, Pergamon Press, London, 1958.
- [21] H.F. Franzen, *Chem. Mater.* 2 (1990) 486.
- [22] C.J. Howard, B.J. Kennedy, P.M. Woodward, *Acta Crystallogr. B* 59 (2003) 463.
- [23] Z. Fang, K. Terakura, J. Kan, *Phys. Rev. B* 63 (1999) 180401–180407.
- [24] L. Rukang, Z. Yingjie, Q. Yitai, C. Zuyao, *Physica C* 176 (1991) 19.
- [25] R. Cava, J. Krajewski, H. Takagi, H. Zanberg, R. Van Dover, W. Peck Jr., B. Hessen, *Physica C* 191 (1992) 237.